Applied Radiation and Isotopes 227 (2026) 112304

Contents lists available at ScienceDirect

Applied Radiation and Isotopes

journal homepage: www.elsevier.com/locate/apradiso

SOLARIS: A neutron tracker feasibility study for the next-generation solar missions detectors

Dimitrios Papanikolaou [a,b], Agatino Musumarra [a,b,*], Nikolaos Patronis [c], Maria Grazia Pellegriti [b], Zinovia Eleme [c], Cristian Massimi [d,e], Riccardo Mucciola [f,g]

[a] DFA, Università di Catania, via S. Sofia n.64, Catania, 95123, Italy
[b] INFN Sezione di Catania, via S. Sofia n.64, Catania, 95123, Italy
[c] Department of Physics, University of Ioannina, Ioannina, 45500, Greece
[d] DFA, Università di Bologna, Bologna, 40127, Italy
[e] INFN Sezione di Bologna, Bologna, 40127, Italy
[f] DIF, Università di Bari, Bari, 70125, Italy
[g] INFN Sezione di Bari, Bari, 70125, Italy

ARTICLE INFO

Keywords:
Neutron tracking
Solar neutron detection
Nuclear astrophysics
Detector characterization
GEANT4 simulation

ABSTRACT

The advancement of neutron detection and imaging technologies in space environments necessitates cutting-edge innovations to develop reliable, low-power, and adaptable detection systems. Recent space missions, such as the Parker Solar Probe and ESA Solar Orbiter, have demonstrated the feasibility of approaching the Sun's outer corona. These missions, have provided novel insights into the plasma dynamics that govern solar wind and flare activity, where high-energy particles are generated and accelerated. In this context, the characterization and mapping of neutron flux have the potential to reveal critical details about the complex interplay of nuclear and plasma processes occurring on the solar surface. To approach this purpose, a next-generation neutron tracker detector is being proposed and simulated. A proof-of-concept setup, designed to combine simplicity with high-performance capabilities, is being studied to evaluate detection efficiency and energy reconstruction capability. The setup has been conceived to incorporate mechanically adjustable features, allowing for high detection efficiency and real-time optimization of neutron-tracking angular resolution.

1. Introduction

Solar neutrons are primarily produced during solar energetic particle events, particularly during solar flares. These neutrons, result mainly from collisions between high-energy protons and ions with the solar atmosphere, accompanied by γ-rays. Solar neutrons offer valuable insights into the production mechanisms of energetic ions during flares (Vilmer et al., 2011). High-energy solar neutrons ($E_n \gg 20$ MeV) have been extensively observed (see Dorman, 2010 for a review of the major investigated solar events). However, detecting low-energy solar neutron flux (less than 10 MeV) presents significant challenges due to the free neutron decay lifetime ($\sim$ 14.67 min), which means nearly all neutrons decay before reaching Earth. Additionally, at Earth's surface, neutron flux is further diminished by atmospheric scattering and absorption, complicating the isolation of signals from those induced by secondary neutrons and cosmic-rays background. As a result, this limits the ability to directly measure the full spectrum of neutron events (Artamonov et al., 2016). Consequently, space-based detectors remain essential for the effective measurement of low-energy solar neutrons, requiring dedicated and complex instrumentation.

1.1. Neutron production mechanisms

Solar flares are primarily driven by magneto-hydrodynamic processes. The emergence of magnetic fields from the solar interior to the atmosphere, the formation of a current sheet, as well as the rapid magnetic reconnection are key processes that lead to the explosive release of energy, heating plasma, and acceleration of particles (Shibata and Magara, 2011).

Solar neutrons are mainly produced through interactions of flare accelerated protons and alpha particles with the solar atmosphere, with significant contributions from ^{3}He reactions (Ligenfelter et al., 1965). The production of neutrons and γ-rays is highly dependent on the energy spectrum and angular distribution of the accelerated ions.

* Corresponding author at: DFA, Università di Catania, via S. Sofia n.64, Catania, 95123, Italy.
E-mail address: agatino.musumarra@unict.it (A. Musumarra).

https://doi.org/10.1016/j.apradiso.2025.112304
Received 17 July 2025; Received in revised form 18 October 2025; Accepted 4 November 2025
Available online 8 November 2025

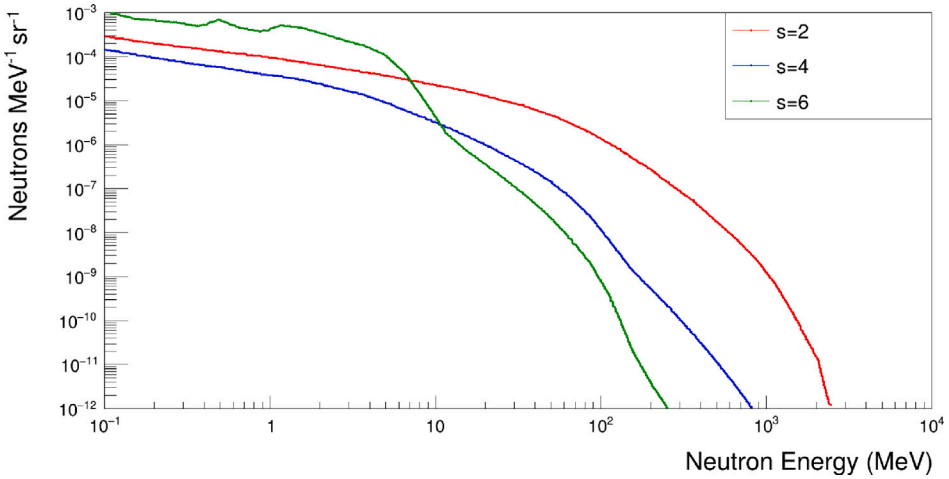

Fig. 1. Total neutron spectra produced, during a disk flare, by accelerated ions in the solar atmosphere after propagating through it, without being affected by neutron decay. The observation line of sight is perpendicular to the solar equatorial plane ($\theta^n_{obs} = 0°$). Spectra are normalized to a proton number N_p (>30 MeV) = 1 and correspond to three different power-law kinetic-energy distributions with spectral indices s = 2, s = 4, and s = 6 (Murphy et al., 2012).

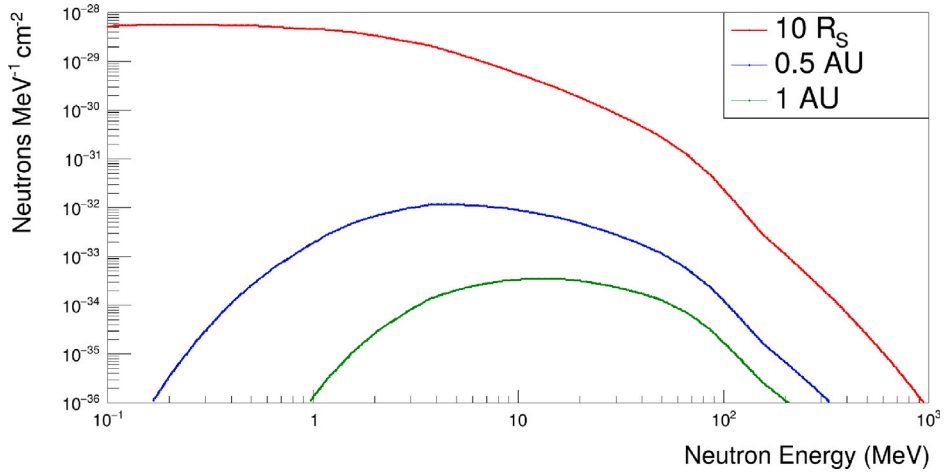

Fig. 2. Time-integrated neutron spectra produced, by a disk flare, from interactions of accelerated ions with the solar atmosphere as seen by an observer located at three different distances from the Sun: 10 R_S (solar radii), 0.5 AU, and 1 AU and $\theta^n_{obs} = 0°$. Spectra are normalized to a number of protons N_p (>30 MeV) = 1. The spectra correspond to a power-law kinetic-energy distribution with spectral index s=4 (Murphy et al., 2012).

Neutron yields from these interactions become significant when energetic ions ($E_{ions} \gg 30$ MeV) are involved, where knock-on reactions in hydrogen and helium dominate over evaporation/spallation in heavier elements (Ligenfelter et al., 1965). A secondary mechanism involves ^{3}He reactions with heavy nuclei, which contribute substantially to neutron production only in flares extremely enriched in^{3}He (^{3}He/^{4}He >1) (Murphy and Kozlovsky, 2017).

Neutron production is also closely linked to γ-ray emissions during solar flares. The 2.223 MeV γ-ray line, resulting from neutron capture on hydrogen, is a key observable, although it is not a reliable measure for high-energy neutron production (Hua and Ligenfelter, 1987; Lockwood et al., 1997).

The produced neutron energy spectra for disk flares (occurring at the Sun's surface), as calculated by Murphy et al. (2012), are shown in Fig. 1. Neutrons are generated from interactions of accelerated ions with the solar atmosphere. Spectra are computed for different ion kinetic-energy distributions, characterized by power-law spectral indices ranging from s = 3 to s = 6, as deduced from analyses of flare data, and include contributions from various nuclear reaction channels. The spectral index s determines the relative abundance of energetic ions: smaller values (harder spectra) indicate a flatter distribution including more high-energy particles capable of producing neutrons, whereas larger values (softer spectra) represent a steeper decline, thus generating a lower neutron yield at higher energies.

Each calculated neutron energy spectrum is normalized to $N_p = 1$ for primary protons with E_p >30 MeV, i.e., it represents the produced yield per single incident proton with energy above this energy threshold. Absolute spectra for a given event can be obtained by multiplying this "per-proton spectrum" by the total number of protons N_p inferred from the data.

This normalization allows for a direct comparison of neutron production efficiencies across different models and observations, being independent of the total number of accelerated protons in a specific solar flare event. These energetic protons (E_p > 30 MeV) are particularly relevant because they have enough energy to interact with nuclei and produce neutrons through nuclear reactions, such as (p,n) or spallation reactions.

As a result of the short lifetime of free neutrons, the neutron flux will depend on the observer distance from the Sun. Estimated time-integrated neutron spectra, produced by a disk flare, as seen by a detector located at three different distances from the Sun: 10 R_S (solar radii), 0.5 AU, and 1 AU are shown in Fig. 2 (Murphy et al., 2012). As expected, the neutron flux exhibits a strong suppression at low energy as the distance from the Sun increases.

Table 1
Examples of neutron detectors developed for low Earth orbit or space missions, organized by neutron energy range. Each entry includes detector type, mission location, and current operational status.

Apparatus	Detector type	Location	Neutron Energy Range	Status
MGNS Spectrometer (Kozyrev et al. (2016))	$CeBr_3$ crystal, ^{3}He tubes and a stilbene scintillator	BepiColombo space mission	From thermal to 10 MeV	Operational
Neutron Spectrometer (Feldman et al. (2010))	Scintillator detectors	MESSENGER space mission	0.5–8 MeV	Operational
DANSON (Benker et al. (2019))	Boron-based detectors	ISS, low Earth orbit	2–4 MeV	Operational
FIB (Muraki et al. (2012))	Plastic scintillators	ISS, low Earth orbit	30–120 MeV	Finished
COMPTEL (McConnell et al. (1993))	Scintillator detector	Compton Gamma Ray Observatory, low Earth orbit	20–150 MeV	Finished
SONTRAC (Nolfo et al. (2019))	Scintillating fibers	For small satellites	High-energy neutrons (20–200 MeV)	Under Development
PAMELA Neutron Detector (Bogomolov et al. (2017))	^{3}He counters	RESURS-DK1 satellite, low Earth orbit	High-energy neutrons (10–1000 MeV)	Finished

In order to estimate a realistic neutron flux at the detection site (Lario (2012)) proposed to normalize the calculated neutron spectrum at the Sun by using the ground-based neutron monitor observations; for this purpose the upper limit of 4.3 10^{28} neutrons MeV^{-1} sr^{-1} at 100 MeV, corresponding to the highest neutron flux at the Sun generated during the 24 May 1990 event was used. The obtained time-integrated neutron flux at E_n=10 MeV and 1 AU distance from the Sun was ~ 100 neutrons MeV^{-1} cm^{-2}.

1.2. Solar neutron detection

Detecting solar neutrons is a complex task involving several experimental techniques. These fall into two primary categories, based on detector location: detectors operating on Earth or in Earth's vicinity, and those installed on spacecrafts involved in dedicated missions closer to the Sun.

Regarding Earth-based and near-Earth detection systems, ground-based neutron monitors (NMs) have been used to indirectly observe high-energy solar neutrons by measuring the secondary radiation produced when these neutrons interact with the Earth's atmosphere (see Dorman, 2010 for review).

In the following, some examples of neutron detectors developed for low Earth orbit satellites or space missions will be described and reported in Table 1.

A first example is the DANSON system (University of Nebraska detector for the analysis of solar neutrons), which utilizes boron-based detectors such as lithium tetraborate ($Li_2B_4O_7$) and boron carbide aboard the International Space Station (ISS) for the detection of low-energy solar neutrons (2–4 MeV range) (Benker et al., 2019). This approach is advantageous in reducing the background produced by the surrounding environment, but results are constrained by the detector location in a low-Earth orbit.

The ancillary neutron detector of the PAMELA mission, which was devoted to the study of cosmic rays (Adriani et al., 2013), operated aboard the Resurs-DK1 satellite, located in low-Earth orbit. This neutron detector was made by two layers of 18 cylindrical ^{3}He proportional counters, enclosed in a polyethylene moderator. It allowed to search for solar neutrons by analyzing 28 solar events that occurred during the 2006–2015 period. Neutrons were detected during time intervals between registrations of charged particle events, enabling continuous solar neutron monitoring (Bogomolov et al., 2017; Goryacheva et al., 2017).

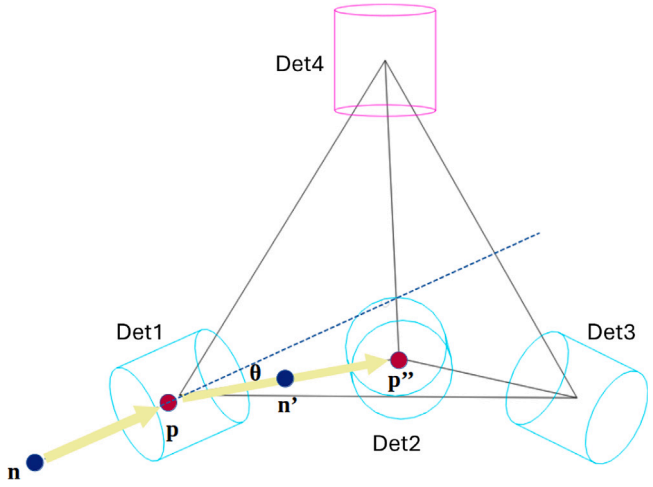

Fig. 3. A simplified schematic representation of the working principle with four cylindrical detectors placed in a regular tetrahedral configuration. Neutron beam is impinging from the left side on Det1, inducing the first scattering. Second scattering is induced in Det2. Det1 detects the first scattered proton, p, and Det2 detects the second scattered proton, p''. θ is the polar angle between the direction of the initial neutron, n, and the scattered neutron, n'.

The Imaging Compton Telescope COMPTEL aboard NASA's Compton Gamma Ray Observatory (CGRO) mission is another comparable example, capable of measuring solar flare neutrons (in the 20–150 MeV range) using scintillators and the neutron double scattering technique (McConnell et al., 1993; McConnell, 1994).

FIBer detector (FIB), launched on board the Space Shuttle Endeavour in 2009 and began collecting data at the ISS, was an interesting device consisting of a plastic scintillator with 32 layers (sheets) capable of determining both the energy and arrival direction of neutrons using *n-p* scattering (Muraki et al., 2012).

The BepiColombo mission, a joint endeavor by ESA and JAXA, aiming to explore Mercury, is equipped with a suite of scientific instruments, including the Mercurian Gamma-Ray and Neutron Spectrometer

Table 2
Comparison of expected and simulated *n–p* events at various neutron energies using different GEANT4 physics lists (1E6 primary neutrons).

Beam Energy (MeV)	Reaction	Expected Counts	Geant4 Counts	Deviation %
QGSP_BERT_HP - 1E6 primaries				
5	$^{1}H(n,el)^{1}H$	224 623	179 381	20.1%
10	$^{1}H(n,el)^{1}H$	110 676	97 078	12.3%
15	$^{1}H(n,el)^{1}H$	75 987	66 922	11.9%
QGSP_INCLXX_HP - 1E6 primaries				
5	$^{1}H(n,el)^{1}H$	224 623	163 620	27.2%
10	$^{1}H(n,el)^{1}H$	110 676	97 119	12.2%
15	$^{1}H(n,el)^{1}H$	75 987	66 860	12.0%
QGSP_BIC_AllHP - 1E6 primaries				
5	$^{1}H(n,el)^{1}H$	224 623	162 872	27.5%
10	$^{1}H(n,el)^{1}H$	110 676	97 140	12.2%
15	$^{1}H(n,el)^{1}H$	75 987	66 898	12.0%

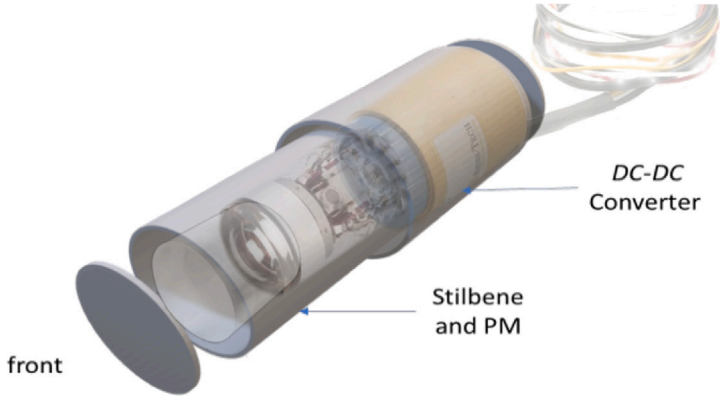

Fig. 4. A schematic representation of the "p-stil" module showing the main detector components: aluminum window, stylbene cylinder, photomultiplier and power supply (DC-DC converter).

(MGNS). The MGNS is provided with an innovative $CeBr_3$ crystal, allowing for precise measurements of γ-rays, three ^{3}He gas-filled tubes and one stilbene organic scintillator crystal. (Mitrofanov et al., 2021; Kozyrev et al., 2020, 2016). The instrument is capable of measuring neutron fluxes across a wide energy range, from thermal energies up to 10 MeV, and γ-rays from 300 keV to 10 MeV (Kozyrev et al., 2020).

Concerning MESSENGER (MErcury Surface, Space ENvironment, GEochemistry, and Ranging) NASA mission designed to study Mercury's surface composition, magnetic field, and exosphere, it utilizes scintillation-based solar neutron detectors (NSs) primarily designed for planetary science, particularly to map surface hydrogen on Mercury. Its reported detection of solar neutrons (Feldman et al., 2010; Lawrence et al., 2014) was heavily debated (Share et al., 2015) due to the inability to distinguish between direct solar neutrons and secondary background neutrons generated by spacecraft interactions.

An interesting neutron detector development is proposed by the SOlar Neutron TRACking (SONTRAC) detector, which is based on scintillating fibers readout by silicon photomultipliers (SiPMs) to detect fast neutrons (between 20–200 MeV). This setup would provide high-resolution imaging of neutron scatters on protons and would be suitable for compact, low-power designs ideal for small satellite platforms (Nolfo et al., 2019).

1.3. Limitations of solar neutron detectors and future perspectives

Despite significant advancements, solar neutron detection remains hindered by several limitations. Challenges primarily include high background, particularly in space-based detectors, where cosmic rays and other ambient radiation can obscure the signals from solar neutrons (Nolfo et al., 2019).

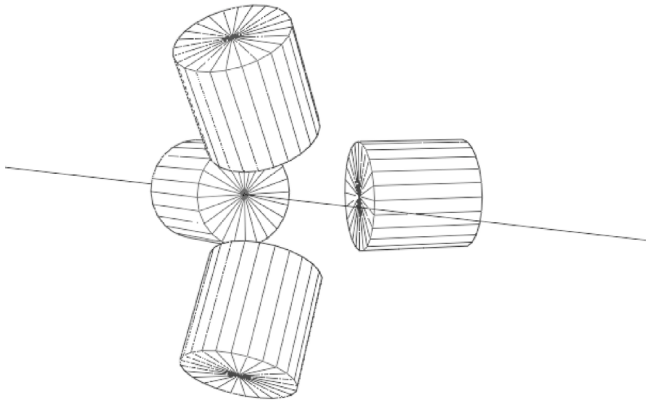

Fig. 5. A simplified version of the prototype setup, simulated using GEANT4. The beam is directed from the rear toward the centroid of the tetrahedral detector configuration.

In this context, the recent success of the Parker Solar Probe, which achieved record-breaking proximity to the Sun surface of about 0.166 AU (Adhikari et al., 2019) is opening new frontiers in the study of solar activities capable of covering a much wider energy spectrum previously unreachable.

Additionally, the need for large-scale detectors to measure time-of-flight or other parameters adds complexity and cost to the detection setups. The detection of high-energy neutrons, remains challenging due to the proton recoil effect, which can lead to the escape of protons from

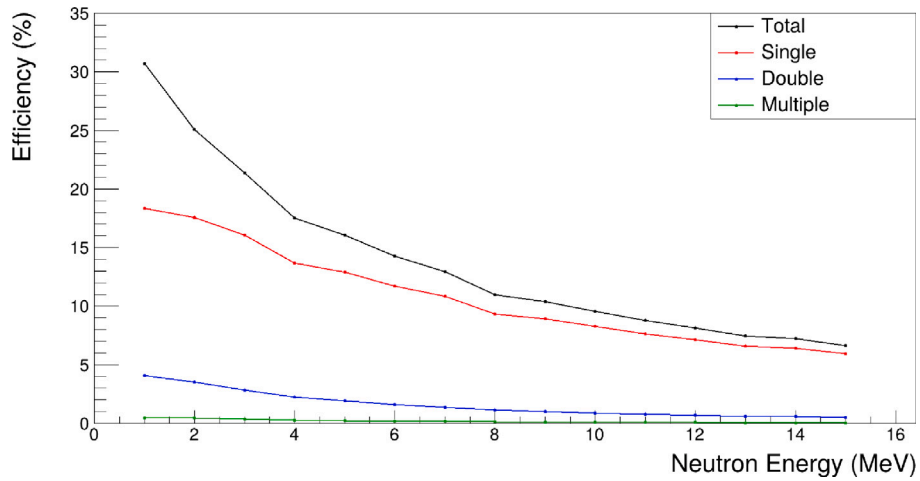

Fig. 6. Neutron detection efficiency of (n,p) events in a single crystal. A detection threshold at 0.1 MeV was applied. "Total" refers to all the (n,p) events recorded; "Single" to events where one scattering occurs; "Double" to events where two scatterings occur; and "Multiple" to events where >2 scatterings occur.

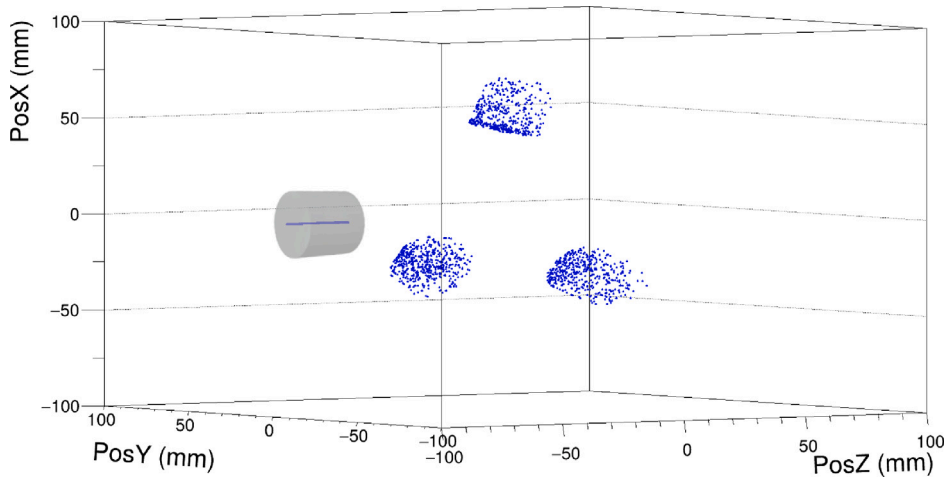

Fig. 7. An example of the interaction points of selected double-scatter (n,p) coincidence events for a 5 MeV pencil neutron beam and 10 cm side length distance. In total, 1E6 primary neutrons were simulated. A sketch of the primary detector is shown. The beam is directed from the left to the right (toward the centroid of the tetrahedral detector configuration; see Fig. 5). A detection threshold at 0.1 MeV was applied.

detectors, thereby degrading both energy and angular resolution (Nolfo et al., 2019).

Instrumentation for solar neutron detection is also constrained by space limitations related to the available volumes. Space-based missions like MESSENGER must fit sophisticated instruments into compact spacecraft, limiting the size and separation of detectors. This results in trade-offs between detector efficiency, spatial and power constraints. Power supply is a critical limitation, as space missions operate with strict energy budgets, often relying on solar panels or radioisotope thermoelectric generators (RTGs). The power requirements for neutron detection instruments typically range from a few Watts to tens of Watts.

As a general remark, scintillator-based technologies used for neutron detection often require high segmentation to achieve sufficient energy resolution, which further increases the complexity and cost of detectors (Nolfo et al., 2019). Finally, the ability to reconstruct neutron momentum would represent a cutting-edge advancement in detection performance, enabling strong suppression of both direct (cosmic rays) and spacecraft-induced background noise.

2. Detector design concept

2.1. Recoil proton track imaging

Recoil proton track imaging (RPTI) has been proposed as a promising technique for fast-neutron spectrometry, with potential applications in nuclear physics and radiation dosimetry. The method aims to reconstruct the neutron momentum by tracking the recoil protons produced by *n-p* elastic scattering when neutrons interact with hydrogen-rich materials. In particular, the technique envisages the use of scintillating materials in which scattered proton trajectories can be captured by using advanced optical imaging systems Hu et al., 2018a,b; Valle et al., 2017; Nolfo et al., 2019; Musumarra et al., 2021; Massimi et al., 2022. In this context, the 3D reconstruction of recoil proton tracks is required for determining the neutron direction and energy, thus allowing full momentum reconstruction.

Among the setups under development described in the literature, the MONDO tracker, (Valle et al., 2017; Marafini et al., 2017; Gioscio et al., 2020), designed for particle therapy treatments, proposes to detect recoil protons through a plastic scintillating fiber matrix, the

produced light being amplified by a triple GEM-based image intensifier or by CMOS SPAD (Single Photon Avalanche Diode) array.

Specifically devoted to neutron detection in space environment, the aforementioned SONTRAC neutron spectrometer, (Nolfo et al., 2019), consists of orthogonally stacked plastic scintillators readout by arrays of SiPMs.

Further developments have been proposed through the RIPTIDE-detector feasibility study for nuclear physics, particle therapy, and dosimetry applications (Musumarra et al., 2021; Massimi et al., 2022, Console Camprini et al., 2023; Pisanti et al., 2024). The proposed system combines a plastic scintillator coupled to imaging devices, based on CMOS technology, or micro channel plate sensors. The purpose is to provide neutron spectrometry capability by stereoscopically imaging the recoil-protons tracks and correlating spatial and time information. This study aims also at enhancing the scalability of RPTI systems, allowing for larger detection volumes, providing also integration of multiple detection modules, thus expanding the applicability of RPTI across different demanding tasks in nuclear physics research and applications.

Although very promising, the RPTI technique currently has several limitations as its relatively low detection efficiency related to the limited detection volumes. Furthermore, typical systems required for RPTI are complex and expensive to implement. This complexity arises from the need for truly advanced imaging technologies requiring ad-hoc optical systems for precise proton track reconstruction in a large active volume. Another problem arises from background discrimination, as it requires accurately distinguishing true proton tracks from spurious ones caused by background noise, such as scattering on carbon and gamma-ray interactions (Mor et al., 2017; Song et al., 2020).

2.2. The SOLARIS detector

While recoil-proton track imaging (RPTI) remains the benchmark for fully reconstructing fast-neutron kinematics, experience with earlier space-borne instruments shows that double-scattering methods, even without full track imaging, can still deliver valuable information. COMPTEL (McConnell, 1994) proved that a scintillator array using two sequential scatters can measure 20–150 MeV solar-flare neutrons, and FIB (Muraki et al., 2012) demonstrated that single n–p scatters suffice to extract both energy and arrival direction. Building on these results, the SOLARIS concept merges the strengths of each approach: it preserves point-like detection modules but exploits n–p elastic scattering to follow individual solar neutrons, aiming to recover their energy with higher precision while avoiding the complexity of full RPTI tracking.

SOLARIS set-up employs a compact, lightweight and low power multi-detector array comprised of trans-Stilbene ($C_{14}H_{12}$) crystals (Di Chicco et al., 2022; Weldon et al., 2020; Zaitseva et al., 2015; Zhou et al., 2022), arranged in an array tailored to detect *n-p* double scattering occurring in different modules. In detail, the core detection mechanism relies on the neutron elastic *(n,el)* reaction occurring first on one of the hydrogenated Trans-Stilbene crystals (primary vertex), followed by the detection of the scattered neutron (secondary vertex) by any of the remaining crystals. Disentangling double-scattering enables the tracking of neutron kinematics based on a two-point interaction mechanism. In the kinematical reconstruction, the Sun's position is treated as a fixed, point-like neutron source, while the deposited proton energy (E_p) is obtained from the first neutron interaction. The proton recoil angle is given by $\theta_p = 90° - \theta_n$ (for $m_p \simeq m_n$), and the direction of the scattered neutron is geometrically defined by the center of mass of the two scintillators. Therefore, as with fixed-target experiments, where the neutron's origin is precisely known, a single n–p scattering event can be used to reconstruct the incident neutron energy:

$$E_n = \frac{E_p}{\cos^2(\theta_p)} = \frac{E_p}{\sin^2(\theta_n)} \quad (1)$$

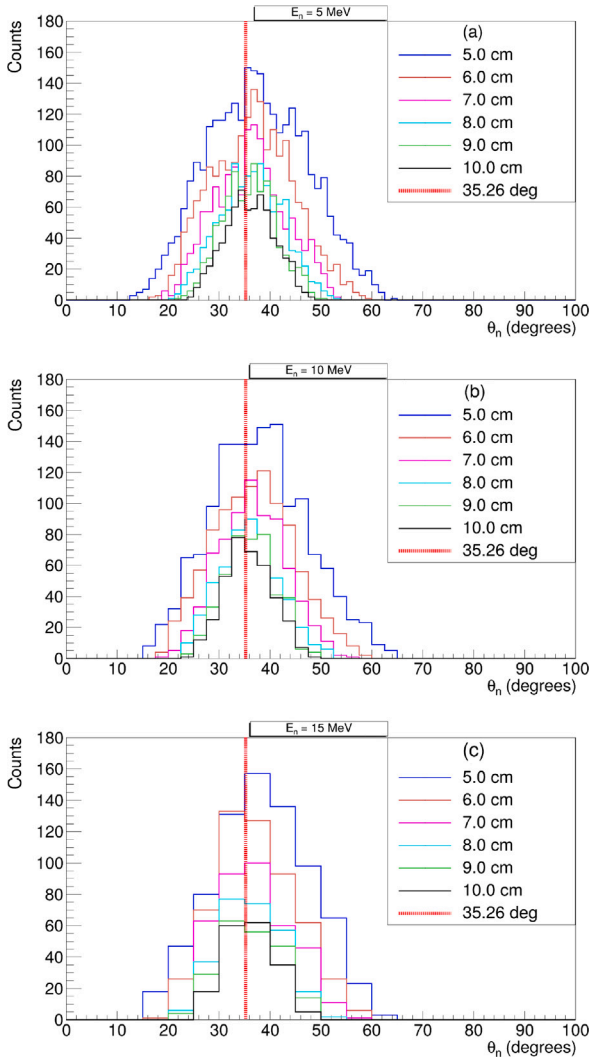

Fig. 8. Angular distributions (polar angles) of the scattered neutron for 5 (a), 10 (b) and 15 (c) MeV beam energy and for 5, 6, 7, 8, 9 and 10 cm side length distances. 1e6 primary neutrons were simulated for every energy and distance pair. The number of bins drops by a factor of 2 in each energy increase. The dotted line is the geometrical angle (35.26°). A detection threshold at 0.1 MeV was applied.

In this approach, only the angle of the first scattered neutron is relevant for determining E_n, while the detailed kinematics of the secondary neutron are not required. The time-of-flight (ToF) of the secondary neutron (n') can serve as an additional kinematical constraint if available.

The configuration enhances the optimization of the secondary neutron direction reconstruction while maintaining a compact and energy efficient detection system. This is achieved by exploiting stilbene's excellent n/γ discrimination capabilities and advanced analysis techniques (Becchetti et al., 2018; Gaughan et al., 2021; Zaitseva et al., 2011, 2020). Stilbene can also effectively discriminate between neutrons and γ-rays - whether originating as secondary emissions from neutron interactions within the crystal or from external sources, such as cosmic rays - making it especially suitable for onboard space applications. A schematic view of the array is depicted in Fig. 3.

The first proof-of-concept prototype includes four solid-state crystals, each measuring ∅1ε × 1ε and characterized by their lightweight, non- hygroscopic, and non-flammable properties, which were assembled into detector modules. They are housed in cylindrical carbon fiber casings with a 50 μm-thick aluminum front window and they

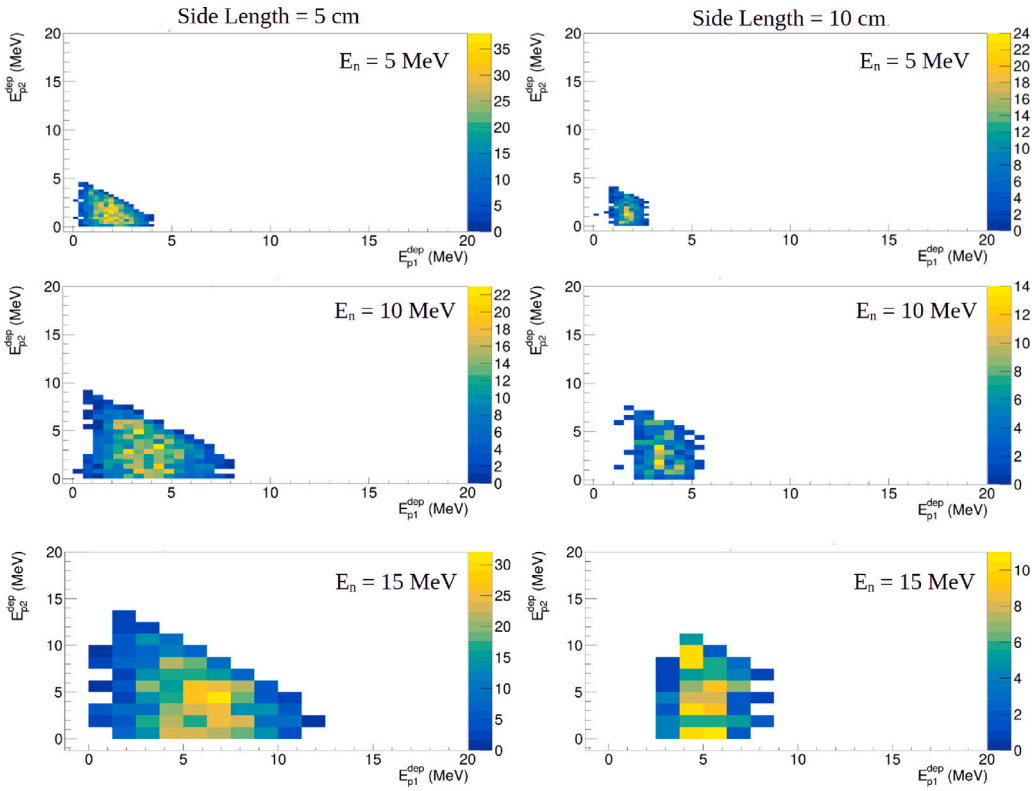

Fig. 9. 2D-histograms of energy depositions of the first vs the second recoil proton for 5 (first row), 10 (second row) and 15 (third row) MeV beam energy and for 5 and 10 cm side length distances. 1E6 primary neutrons were simulated for every energy and distance pair. The number of bins drops by a factor of 2 in each energy increase. A detection threshold at 0.1 MeV was applied.

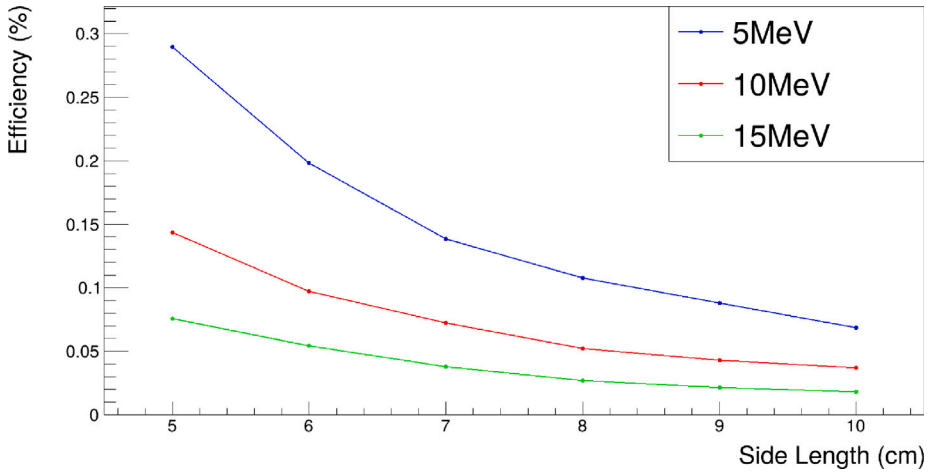

Fig. 10. Total efficiency, in percentage, of (*n,p*) coincidence events as a function of side length at 5, 10 and 15 MeV beam energies. A detection threshold at 0.1 MeV was applied.

are optically coupled to an R7378 A Hamamatsu Photomultiplier Tube (PMT), connected to a PS1807-Sens-Tech active base integrating a DC-DC converter. The compact power base was evaluated as a low-voltage, high-counting rate solution (less than 0.5 W/module power consumption). A schematic representation of the detector modules is provided in Fig. 4.

It is important to highlight that these detectors are currently utilized at the n_TOF/CERN neutron facility (Patronis and Mengoni, 2023) for neutron capture (*n, γ*), neutron elastic (*n,el*), and inelastic scattering (*n,inl*) measurements. This extensive deployment underscores that the modules have been tested and characterized under various experimental conditions, further validating their reliability and performance (Castelluccio et al., 2024; Czakoj et al., 2024; Musumarra et al., 2024; Zaitseva et al., 2020).

Consequently, the characterization was conducted through various performance metrics, including rise-time and fall-time measurements, pulse-height and charge spectra analysis, including Pulse Shape Discrimination (PSD) analysis as reported in (Cieślak et al., 2017; Ferrulli et al., 2021; Papanikolaou, 2024; Papanikolaou et al., 2025; Zaitseva et al., 2011; Gaughan et al., 2021).

3. GEANT4 simulations: Results & discussion

3.1. Introduction

To assess the performance of SOLARIS, a preliminary simulation study was conducted using GEANT4 (Agostinelli et al., 2003), a well-established Monte Carlo toolkit for particle transport in matter. The study primarily focused on evaluating the efficiency of (*n-p*) events, particularly those leading to double-scatter interactions, where a neutron undergoes an initial interaction in the primary crystal and a subsequent interaction in one of the three detection crystals.

In this initial evaluation process, a simplified geometry was employed, consisting solely of the trans-stilbene crystals. A monoenergetic "pencil" neutron beam was directed at the primary detector (active target) to assess its fundamental response characteristics. This setup allowed for a focused investigation of the prototype's performance before introducing additional complexities such as surrounding materials, background radiation, or extended geometries. The aforementioned geometry is shown in Fig. 5.

For reference, three high-precision physics lists were primarily tested to evaluate their performance: QGSP_BERT_HP, QGSP_BIC_AllHP, and QGSP_INCLXX_HP. All these models are based on the Quark-Gluon String Model (QGSP), which is well-suited for simulating hadronic interactions, particularly in the low to mid-MeV energy region (up to 20 MeV).

These physics lists incorporate different approaches to intra-nuclear cascade and pre-equilibrium modeling, influencing neutron transport and interaction accuracy within the detector setup. Among the three physics lists tested, QGSP_BERT_HP demonstrated the best performance based on the comparison between theoretically expected and Geant4-reconstructed statistics of (*n-p*) events. The expected values were derived using the following approximation (Eq. (2)):

$$N_{\text{exp}} \approx N_0 \cdot N_t \cdot \sigma(E_i) \tag{2}$$

where N_0 is the beam intensity, N_t the number of target nuclei (^{1}H) per cm^2, and $\sigma(E_i)$ is the microscopic cross-section at a given energy. The above relation is valid when $N_t \cdot \sigma(E_i) \ll 1$.

The reconstructed values were obtained by selecting the relevant (*n,p*) events from the GEANT4 simulation. Both calculations were performed considering a 2.54 cm thick stilbene crystal (single crystal) and a monoenergetic neutron beam. The results are summarized in Table 2 and Fig. 6:

3.2. Multi-detector setup metrics

Once the Monte Carlo (MC) simulation was validated for a single module, the study was extended to the full multi-detector setup, shown in Fig. 5. The goal was to evaluate its effectiveness in capturing double-scatter (*n,p*) coincidence events in the 3 pairs of detectors (as shown in Fig. 7). A detection threshold at 0.1 MeV, was applied for the deposited energy of both recoil protons. In the simulation, a pencil n-beam impinges co-axially on the first detector (primary) along the *z*-axis.

As described in Eq. (1), two key metrics are needed to reconstruct the incident neutron's energy spectrum: the neutron's scattering angle (θ_n) after the first (*n-p*) event in the primary detector, which is fixed by geometrical constraints, and the deposited energy of the recoil proton (E_p). The angular distributions (polar angles) of the detected scattered neutron for various n-beam energies and tetrahedral side lengths (i.e., detector spacing) are reported in Fig. 8.

A crucial aspect of the simulation involved the establishment of a concrete foundation of the working principle, starting from validating the accurate reconstruction of kinematics to defining the range of recovered energies. Since, in a real experiment, both the primary and the scattered neutrons are detected through the energy deposited by the recoil proton, examining the 2D-histogram of their deposited energy provides a solid reference range for energy determination of our observable metric. The distributions of the proton recoil deposited energies for various beam energies and side lengths are showcased in Fig. 9.

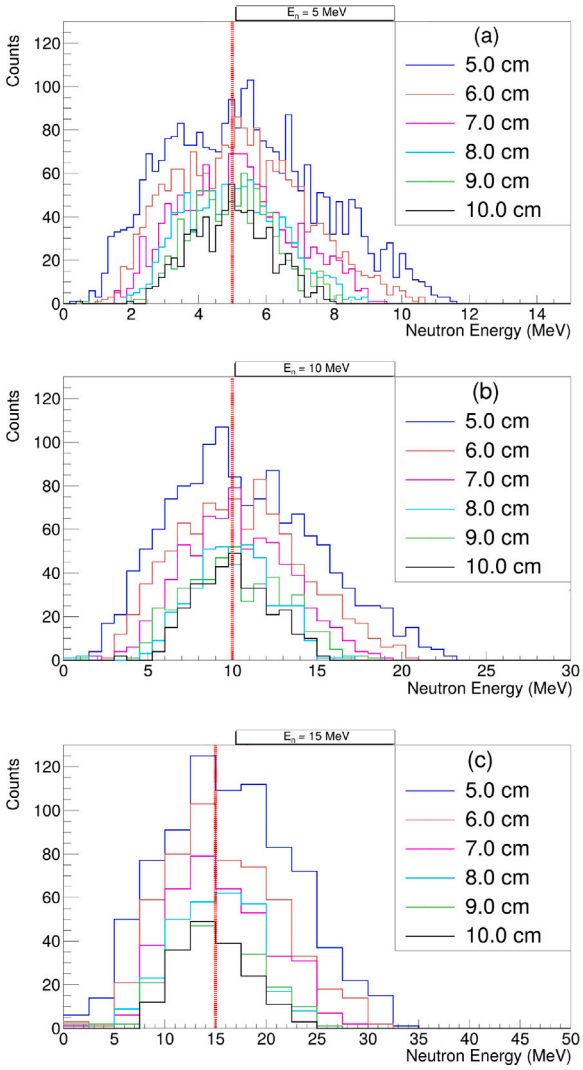

Fig. 11. Reconstructed energy distributions, using angle distributions, for "true" beam energy of 5 (a), 10 (b) and 15 (c) MeV and for 5, 6, 7, 8, 9 and 10 cm side length distances. 1e6 primary neutrons were simulated for every energy and distance pair. The number of bins drops by a factor of 2 in each energy increase. A detection threshold at 0.1 MeV was applied.

As a final remark on Fig. 9, it should be mentioned that the few bins in the low-energy region correspond to events where the secondary proton is produced near the surface of the crystal. In these cases, the proton may escape the detector volume, depositing only a portion of its kinetic energy - just enough to be detected (>0.1 MeV threshold). These events contribute to a very low percentage of the total (*n-p*) coincidence events recorded (ranging from $\sim$ 0.04% to $\sim$ 1.50% depending on the beam energy). The main objective is to determine the optimal detector geometry that balances double-scattering angular resolution and detection efficiency. As the tetrahedral configuration spacing increases, the angular resolution of the (n–p) coincidence events improves, allowing for more precise neutron energy reconstruction (Eq. (1)). However, this comes as expected at the cost of reduced efficiency, as a larger spacing between detectors decreases the probability of capturing multi-scatter events. The effect of varying the side length distance on detection efficiency at various beam energies is illustrated in Fig. 10.

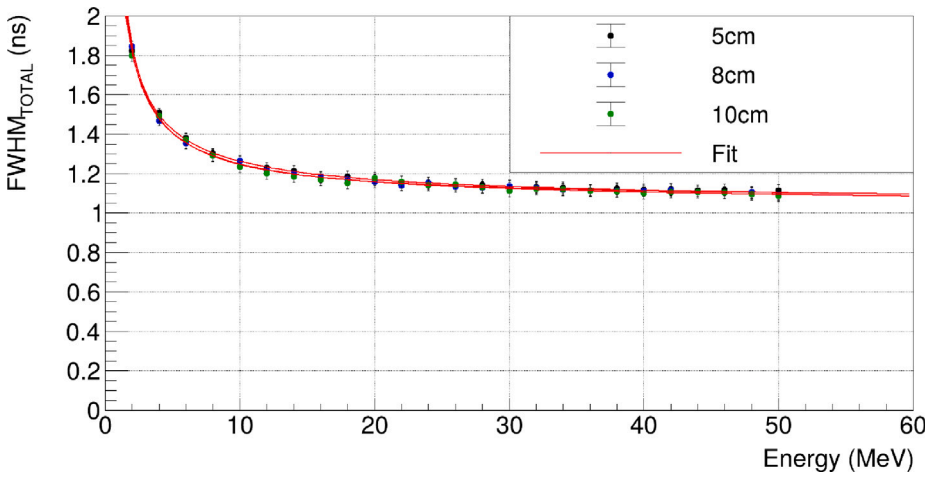

Fig. 12. Figure 12: FWHM$_{TOTAL}$ as a function of incident neutron energy for 5 cm, 8 cm, and 10 cm tetrahedral side lengths. The fitted red lines correspond to the power-law model ($f(E) = a \cdot E^{-b} + c$), with coefficients ((a, b, c)) = (1.36, 0.79, 1.04), (1.45, 0.88, 1.06), and (1.34, 0.80, 1.04) for the 5, 8, and 10 cm cases, respectively. The three curves are nearly coincident due to the weak dependence on detector spacing.

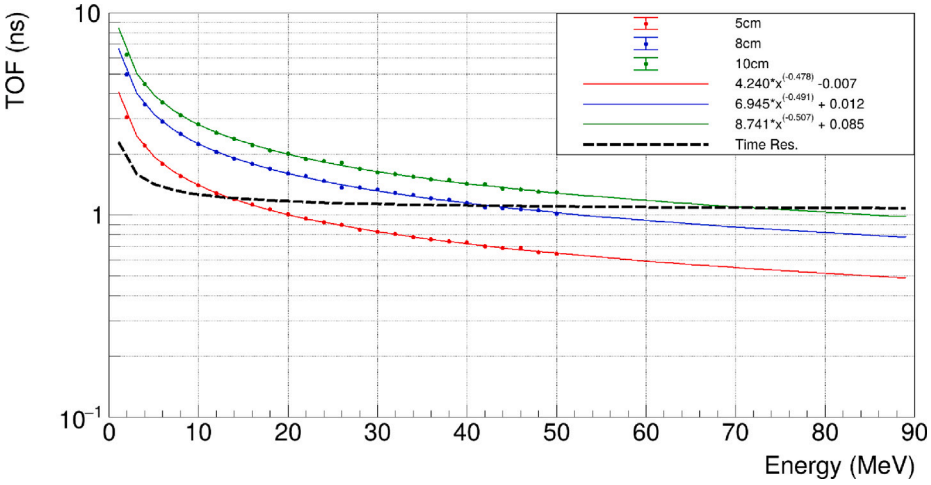

Fig. 13. Average ToF as a function of incident neutron energy and the corresponding time resolution function derived from Fig. 12, denoted as "Time Res". Calculations were performed for 5, 8, and 10 cm side lengths, using ToF distributions up to 50 MeV neutron-beam energies. The same power-law function ($(f(E) = a \cdot E^{-b} + c)$) was used for fitting, as indicated in the legend. The fitted curves were extrapolated up to 90 MeV for reference.

To address the above trade-off, we aim to introduce adaptive mechanical features that enable dynamic adjustments to the detector configuration. By modifying the detector spacing in real-time, the system can optimize either resolution or efficiency depending on the incident neutron flux, ensuring greater flexibility and improved measurement accuracy. After evaluating the above metrics, we can now present the reconstructed incident neutron energy spectra, thus validating the working principle of our detection system. Using the average mean angle (37.79°, 36.98°, 36.50°, 36.11°, 36.01° and 35.90° for 5, 6, 7, 8, 9 and 10 cm respectively) from the distributions of Fig. 8 and the deposited energy of the first recoil-proton, we can apply Eq. (1) to retrieve the neutron energy distributions, reconstructed for various initial beam energies and side lengths, as shown in Fig. 11.

3.3. Time-of-flight analysis and background suppression

To fully characterize the neutron interactions within the SOLARIS array, a complementary analysis was performed on the Time-of-Flight (ToF) distributions for the scattered neutrons detected in coincidence. These distributions serve a twofold purpose by improving background rejection and by enhancing kinematic constraints on the detected neutron events.

As discussed above, a key challenge in neutron detection is the suppression of background contributions, especially when (in a real scenario) the detector array is exposed to an ambient neutron field. By selecting neutron energies where n-p forward scattering complies with the expected ToF distributions, we can identify and eliminate events that do not follow the expected kinematic behavior. The ToF spectra allow us to further isolate true *n-p* coincidence events, reducing background contamination and thus improving the signal-to-noise ratio.

A critical comparison is made between the minimum ToF (high neutron energies) and the timing resolution of the detectors. The timing resolution has two main contributions. First, the ToF spread due to the finite size of the two detectors in coincidence, which can be evaluated from the ToF spectra (as the FWHM of the distribution) and is the dominant factor at low energies and side length distances. Second, the intrinsic time resolution of a single detector, which is a fixed value of ~ 0.75 ns (Papanikolaou, 2024), dominating at higher energies. By combining the FWHM$_{TOF}$ and FWHM$_{Intrinsic}$ (where FWHM$_{Intrinsic}$ = Time Res. $\cdot \sqrt{2}$), as in Eq. (3), a quantifiable way to extrapolate the effect of energy and side length on time resolution, can be obtained (Fig. 12).

$$\mathrm{FWHM}_{\mathrm{TOTAL}} = \sqrt{\mathrm{FWHM}_{\mathrm{TOF}}^2 + \mathrm{FWHM}_{\mathrm{Intrinsic}}^2} \tag{3}$$

Beyond a certain neutron energy, the ToF resolution becomes comparable to the timing resolution, making it impossible to distinguish coincidences. Fig. 13 illustrates a "rough" upper energy limit beyond which neutron interactions cannot be reliably resolved using timing techniques. This provides an essential reference for setting energy cut-offs in future analyses. "TOF" in Fig. 13 refers to the average value of the ToF distributions for various side lengths and n-beam energies (data points up to 50 MeV, with fitted functions extrapolated to 90 MeV).

In practice, the situation is more complex. A direct comparison between the average ToF and the intrinsic time-resolution functions only provides an upper theoretical limit for coincidence discrimination. To realistically assess detector performance, one must convolute the ToF distribution with the detector time-resolution function. This will determine the fraction of coincidence events that can still be correctly identified when background or ambient neutron fields are present. Experimentally establishing an acceptable overlap threshold is therefore essential to ensure reliable event separation under realistic operating conditions.

As mentioned above, definitively determining an upper energy limit based on the intersection point of the two functions would be problematic, as the actual energy cutoff is lower. However, quantifying these intersection points for the 5 cm case ($\sim$ 13.5 MeV), the 8 cm case ($\sim$ 42.8 MeV), and the 10 cm case ($\sim$ 72.8 MeV) can provide a "rough" upper perspective for future experimental applications. Evaluating intermediate side lengths would further refine the understanding of the geometry-dependent energy limits.

Additionally, the ToF distributions provide an independent method for reconstructing the secondary neutron energy (*n'*). By using the ToF of *n'*, the fixed side-length determined by the geometry, the deposited energy of the recoil proton (*p'*), and applying energy conservation in the first interaction site (primary detector), we obtain a second method for reconstructing the initial neutron energy. This offers a complementary constraint on the initial neutron energy reconstruction. These spectra are presented in Fig. 14.

This enables a more precise determination of the neutron flux while further rejecting background events that do not conform to expected energy distributions. By combining all the aforementioned kinematic constraints, including those derived from scattering-angle and deposited-energy correlations, Time-of-Flight analysis, and detector timing resolution, a more robust selection of valid coincidence events can be achieved, thereby enhancing the overall reliability of the reconstructed neutron flux.

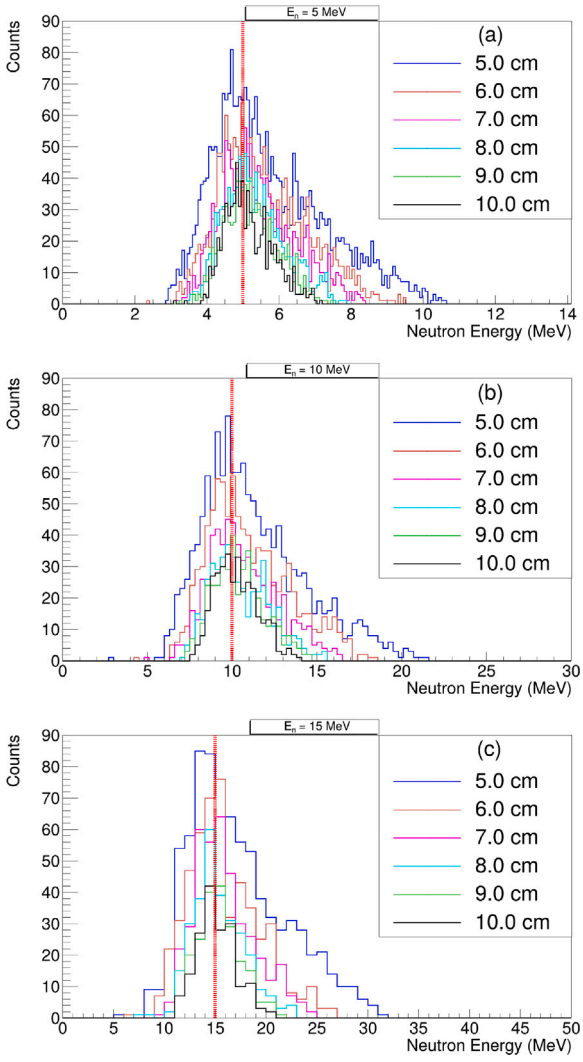

Fig. 14. Reconstructed energy distributions, using ToF distributions, for "true" beam energy of 5 (a), 10 (b) and 15 (c) MeV and for 5, 6, 7, 8, 9 and 10 cm side length distances. 1e6 primary neutrons were simulated for every energy and distance pair. The number of bins drops by a factor of 2 in each energy increase. A detection threshold at 0.1 MeV was applied.

4. Coincidence rate validation by Am-Be n-source

In order to verify the GEANT4 simulations and to assess the coincidence rate by a realistic neutron flux, we performed a first experimental characterization of SOLARIS by using an Am-Be n-source. The measurement was performed at CERN, close to the EAR1 experimental hall (GEAR station) of the n_TOF neutron facility (Patronis and Mengoni, 2023). The Am-Be source had a nominal activity of 350 MBq. The experimental setup (tetrahedron) was placed horizontally and the source was placed on the back of first detector, as shown in Fig. 15. This geometric arrangement maintained cylindrical symmetry with respect to the primary triggering detector. The distance between the center of the source and the center of the stilbene crystal (primary detector) was set to 17.4 cm. According to the geometric arrangement used in the simulations, all detectors had a center-to-center crystal distance of 6 cm. In Fig. 15, the low-voltage distribution-equalizer box is also shown (on the left).

The signals from the four SOLARIS modules were acquired by using an 8-channel CAEN digitizer model DT5743 at a sampling rate of 1.6 GHz. The digitizer's internal trigger was configured to record all events in the primary detector, as well as coincidence events between it and the three ancillary detectors. The cylindrical symmetry of the setup allowed the collection of coherent coincidence rate events in three different pairs of detectors, granting a geometrical consistency check and redundancy for the measured coincidence rates.

Fig. 16 displays the four n/γ PSD 2D-plots, including the total statistics collected in the first detector and the coincidence events measured in the three ancillary detectors. All detectors were calibrated using Cs-137 and Co-60 gamma sources, with a 100 keVee energy threshold applied to all four. The top-left plot in both Fig. 16 and Fig. 17 corresponds to the detector closest to the source, consistent with the arrangement illustrated in Fig. 15.

A designated graphical boundary for neutrons selection was applied to each PSD 2D-plot as shown in Fig. 17. According to the experimental setup and data analysis, the percentage of n,p coincidence events (in regards to the total neutron-induced events detected in the primary detector above the threshold) was 0.93% and, at the same time, the coincidence statistics collected in each pair of modules were found to be consistent.

In order to verify the experimental result a point-like Am-Be n/γ isotropic source was introduced in the GEANT4 simulations. The simulated geometrical arrangement of the four crystals matched the experimental setup. As already stated in the previous sections, the simulation

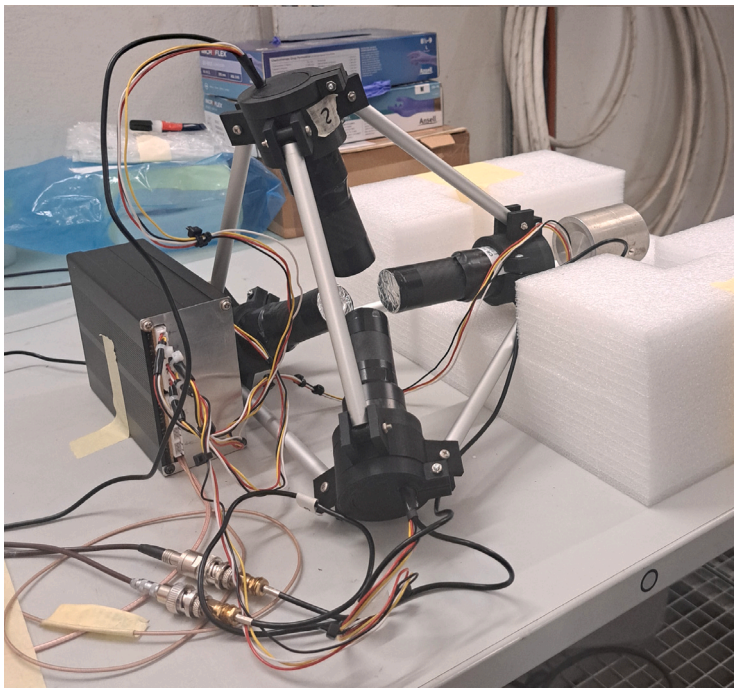

Fig. 15. The test-bench of the SOLARIS setup. The four stilbene detectors were maintained in a regular tetrahedral configuration and the Am-Be source holder was collinear with the first detector.

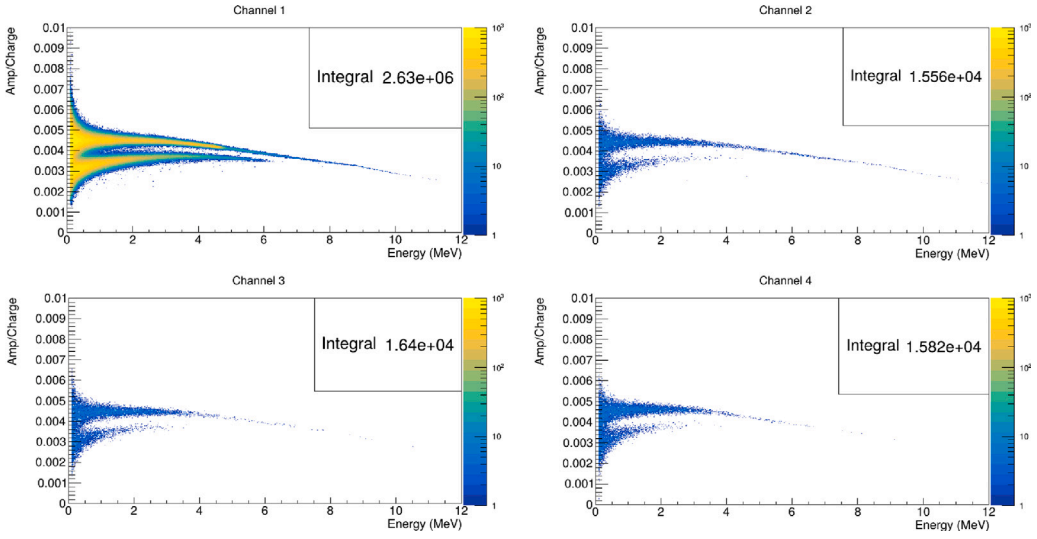

Fig. 16. The four SOLARIS n/γ discrimination plots Amplitude/Charge vs Energy.

included just the scintillator crystals, neglecting the presence of the Photomultipliers, DC-DC converters and carbon fiber holders. Consequently, in order to perform a comparison between experimental data and the simulation, only events where the first detector was firing above an energy threshold of 100 keVee were considered. By directly comparing the simulated Am-Be neutron spectra with the experimental results, the energy threshold was precisely determined. This provided comprehensive control over the energy release in the scintillator.

For comparison with the experimental Am–Be neutron data, the simulated deposited energies were converted to light-output units (MeVee) using the scintillator's quenching function. This approach ensures a consistent threshold definition and allows a direct, physically meaningful comparison between simulated and experimental neutron spectra (Fig. 18).

A total number of 2E9 primary neutrons produced 657319 scattering events above the threshold (0.1 MeVee) on the primary detector. In turn, they produced a total of 4298 coincidence scattering events above threshold on the three ancillary detectors. Therefore, the simulated efficiency with respect to the total neutron-induced events detected in the primary detector was 0.65%. The observed 30% discrepancy between experimental and simulated efficiency could be attributed to the exclusion of multi-scattering (n,p) events, as well as any (n,12C) kinematically possible coincidence combination, in the simulation.

5. Conclusions

The development of SOLARIS represents a further step in neutron detection technology tailored for solar space missions. Through

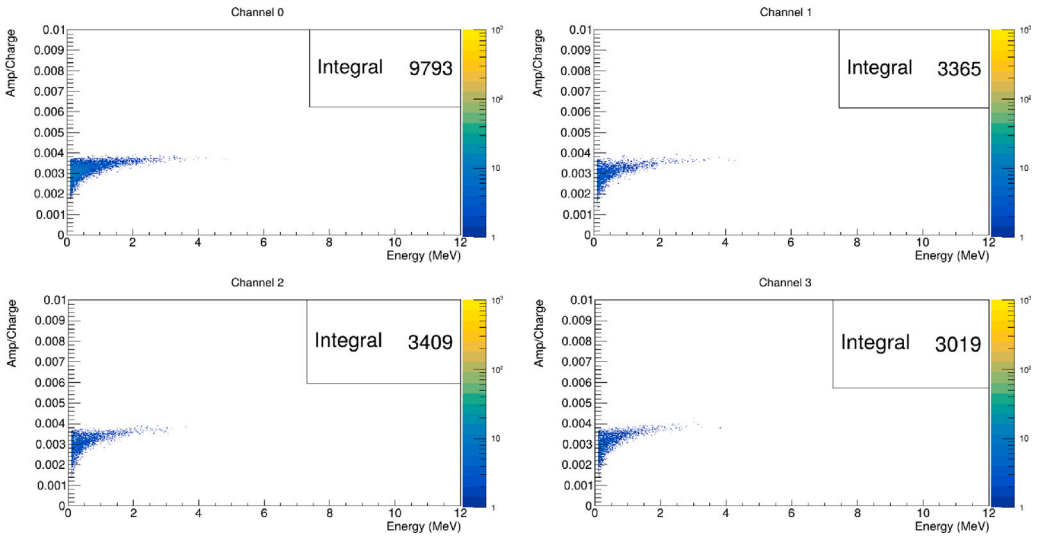

Fig. 17. Final coincidence statistics selecting neutrons in all the detectors. A 100 keVee energy threshold was used for selecting coincidences.

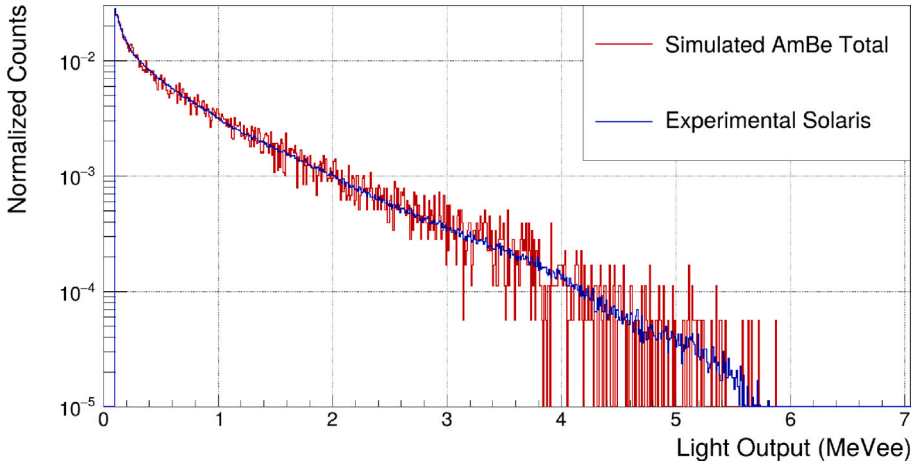

Fig. 18. Am-Be neutron energy spectra: Simulation vs Experiment (normalized so their total integral equals 1). The matching between the two spectra was used to coherently assess the 100 keVee threshold to be used in selecting coincidence events for both experimental and simulated released energy.

comprehensive GEANT4 simulations, we have established the working principle of our prototype by using double-scatter (*n-p*) coincidence events as key mechanism for neutron energy reconstruction. This includes analyzing efficiency, angular and ToF distributions, and energy spectra associated with neutron interactions in stilbene crystals. Validation of the predicted efficiency by an Am-Be neutron source revealed good agreement between experimental results and simulations.

As we progress toward integrating adaptive features into SOLARIS, we anticipate enhanced capabilities for real-time optimization. To balance the trade-off between angular resolution and efficiency, we plan to incorporate adaptive mechanical features that enable real-time adjustments to the detector configuration. By altering the detector spacing based on the incident neutron flux, the system can optimize either resolution or efficiency, enhancing accuracy and adaptability for various experimental conditions.

Moving forward, we plan to extend our simulation to a mixed-energy neutron beam, incorporating more complex and realistic neutron flux models. These simulations will enable us to better evaluate SOLARIS's performance under actual operational conditions, refining the system's capabilities substantially and ensuring that it meets its potential for solar physics research. Future work will focus on refining simulation parameters and validating experimental results to optimize the SOLARIS prototype and guarantee its effectiveness in space-based applications.

CRediT authorship contribution statement

Dimitrios Papanikolaou: Writing – original draft, Validation, Methodology, Investigation, Formal analysis, Data curation, Conceptualization. **Agatino Musumarra:** Writing – review & editing, Validation, Supervision, Project administration, Methodology, Investigation, Funding acquisition, Formal analysis. **Nikolaos Patronis:** Writing – review & editing, Validation, Supervision, Methodology, Investigation, Conceptualization. **Maria Grazia Pellegriti:** Writing – review & editing, Validation, Supervision, Methodology, Formal analysis, Data curation, Conceptualization. **Zinovia Eleme:** Writing – review & editing, Validation, Methodology, Investigation, Data curation. **Cristian Massimi:** Writing – review & editing, Methodology, Formal analysis, Data curation. **Riccardo Mucciola:** Writing – review & editing, Investigation, Data curation, Conceptualization.

Declaration of competing interest

The authors declare that they have no known competing financial interests or personal relationships that could have appeared to influence the work reported in this paper.

Data availability

Data will be made available on request.

References

Adhikari, L., Zank, G., Zhao, L., Kasper, J., Korreck, K., Stevens, M., Case, A., Whittlesey, P., Larson, D., Livi, R., Klein, K., 2019. Turbulence transport modeling and first orbit parker solar probe (PSP) observations. Astrophys. J. Suppl. Ser. 246, 38. http://dx.doi.org/10.3847/1538-4365/ab5852.

Adriani, O., Barbarino, G.C., Bazilevskaya, G.A., et al., 2013. Time dependence of the proton flux measured by PAMELA during the 2006 July–2009 December solar minimum. Astrophys. J. 765, 91, https://iopscience.iop.org/article/10.1088/0004-637X/765/2/91.

Agostinelli, S., et al., 2003. Geant4—a simulation toolkit. Nucl. Instrum. Methods Phys. Res. 506, 250–303. http://dx.doi.org/10.1016/S0168-9002(03)01368-8.

Artamonov, A., Kovaltsov, G., Mishev, A., Usoskin, I., 2016. Neutron monitor yield function for solar neutrons: A new computation. J. Geophys. Res.: Space Phys. 121, 117–128. http://dx.doi.org/10.1002/2015JA021993.

Becchetti, F.D., Torres-Isea, R.O., Di Fulvio, A., Pozzi, S.A., Nattress, J., Jovanovic, I., Febbraro, M., Zaitseva, N., Carman, L., 2018. Deuterated stilbene (stilbene-d12): An improved detector for fast neutrons. Nucl. Inst. Methods Phys. Res. A 908, 376–382. http://dx.doi.org/10.1016/j.nima.2018.08.021.

Benker, N., Echeverria, E., Olesen, R., Kananen, B., McClory, J., Burak, Y., Adamiv, V., Teslyuk, I., Peterson, G., Bradley, B., Wilson, E., Petrosky, J., Dong, B., Kelber, J., Hamblin, J., Doumani, J., Dowben, P., Enders, A., 2019. Possible detection of low energy solar neutrons using boron-based materials. Radiat. Meas. 129, 106190. http://dx.doi.org/10.1016/j.radmeas.2019.106190.

Bogomolov, E., Adriani, O., et al., 2017. Bull. Russ. Acad. Sci.: Phys. 132–135. http://dx.doi.org/10.3103/S1062873817020113.

Castelluccio, D.M., Camprini, P.C., Diakaki, M., Eleme, Z., Massimi, C., Mastromarco, M., Mucciola, R., Musumarra, A., Patronis, N., Pellegriti, M.G., Sahoo, R.N., the n_TOF Collaboration, 2024. Response of stilbene scintillator to (n, n) and (n, n'). https://cds.cern.ch/record/2894839/files/INTC-I-274.pdf.

Cieślak, M.J., Gamage, K.A., Glover, R., 2017. Pulse shape discrimination characteristics of stilbene crystal, pure and 6Li loaded plastic scintillators for a high resolution coded-aperture neutron imager. J. Instrum. 12, P07023. http://dx.doi.org/10.1088/1748-0221/12/07/P07023.

Console Camprini, P., Leone, F., Massimi, C., Musumarra, A., Pellegriti, M., Pisanti, C., Romano, F., Spighi, R., Terranova, N., Villa, M., 2023. A proton-recoil track imaging system for fast neutrons: the RIPTIDE detector. J. Instrum. 18, C01054. http://dx.doi.org/10.1088/1748-0221/18/01/C01054.

Czakoj, T., Košťál, M., Novák, E., Losa, E., Šimon, J., Schulc, M., Mravec, F., Cvachovec, F., Rataj, J., Matěj, Z., 2024. Measurement of prompt neutron capture gamma coming from iron and chlorine. Ann. Nucl. Energy 198, 110317. http://dx.doi.org/10.1016/j.anucene.2023.110317.

Di Chicco, A., Sardet, A., Petit, M., Jacqmin, R., Gressier, V., Stout, B., 2022. Gamma-response characterization of a solution-grown stilbene based detector assembly in the 59 keV – 4.44 MeV energy range; an alternative low-resolution gamma spectrometer. Nucl. Instrum. Methods Phys. Res. A 1034, 166740. http://dx.doi.org/10.1016/j.nima.2022.166740.

Dorman, L., 2010. Solar Neutrons and Related Phyenomena. Astrophysics and Space Science Library. Springer, https://link.springer.com/book/10.1007/978-90-481-3737-4.

Feldman, W.C., Lawrence, D.J., Goldsten, J.O., Gold, R.E., Baker, D.N., Haggerty, D.K., Ho, G.C., Krucker, S., Lin, R.P., Mewaldt, R.A., Murphy, R.J., Nittler, L.R., Rhodes, E.A., Slavin, J.A., Solomon, S.C., Starr, R.D., Vilas, F., Vourlidas, A., 2010. Evidence for extended acceleration of solar flare ions from 1–8 MeV solar neutrons detected with the MESSENGER neutron spectrometer. J. Geophys. Res. 115, A01102. http://dx.doi.org/10.1029/2009JA014535.

Ferrulli, F., Dinar, N., Manzano, L.G., Labalme, M., Silari, M., 2021. Characterization of stilbene and EJ-276 scintillators coupled with a large area SiPM array for a fast neutron dose rate detector. Nucl. Instrum. Methods Phys. Res. A 1010, 165566. http://dx.doi.org/10.1016/j.nima.2021.165566.

Gaughan, N., Zhou, J., Becchetti, F.D., Torres-Isea, R.O., Febbraro, M., Zaitseva, N., Altmann, Y., Di Fulvio, A., 2021. Characterization of stilbene-d12 for neutron spectroscopy without time of flight. Nucl. Inst. Methods Phys. Res. A 1018, 165822. http://dx.doi.org/10.1016/j.nima.2021.165822.

Gioscio, E., Battistoni, G., Bochetti, A., De Simoni, M., Dong, Y., Fischetti, M., et al., 2020. Development of a novel neutron tracker for the characterisation of secondary neutrons emitted in particle therapy. Nucl. Instrum. Methods Phys. Res. Sect. A: Accel. Spectrometers Detect. Assoc. Equip. 958, 162862. http://dx.doi.org/10.1016/j.nima.2019.162862.

Goryacheva, V., Voronov, S., Mikhailov, V., 2017. Method of solar neutron search with PAMELA neutron detector. J. Phys.: Conf. Ser. 798, http://dx.doi.org/10.1088/1742-6596/798/1/012039.

Hu, J., Liu, J., Zhang, Z., Chen, L., Guo, Y., He, S., Xu, M., Zhou, L., Yao, Z., Yuan, X., Zhang, Q., Ouyang, X., 2018a. Recoil-proton track imaging as a new way for neutron spectrometry measurements. Sci. Rep. 8, 13363. http://dx.doi.org/10.1038/s41598-018-31711-z.

Hu, J., Zhang, Z., Chen, L., Liu, J., Yan, M., Zhao, K., He, S., Xu, M., Zhou, L., Jin, P., Ouyang, X., 2018b. Determination of fast neutron spectrum using recoil-proton track imaging method. J. Instrum. 13, P06010. http://dx.doi.org/10.1088/1748-0221/13/06/P06010.

Hua, X., Ligenfelter, R., 1987. Solar flare neutron production and the angular dependence of the capture gamma-ray emission. Sol. Phys. 107, 351–383. http://dx.doi.org/10.1007/BF00152031.

Kozyrev, A., Litvak, M., Malakhov, A., Mitrofanov, I., Mokrousov, M., Sanin, A., Tretiyakov, V., Owens, A., Schulz, R., Quarati, F., 2020. Spectroscopy of gamma-rays of Earth, Venus and Mercury: MGNS instrument onboard BepiColombo mission. In: EGU General Assembly 2020, Online, 4–8 2020. EGU2020-9657, http://dx.doi.org/10.5194/egusphere-egu2020-9657.

Kozyrev, A., Mitrofanov, I., Benkhoff, J., Owens, A., Quarati, F., Litvak, M., Malakhov, A., Mokrousov, M., Timoshenko, G., Shvetsov, V., 2016. Next generation of scintillation detector based on cerium bromide crystal for space application in the gamma-ray spectrometer of the mercurian gamma-ray and neutron spectrometer. Instrum. Exp. Tech. 59, 569–577. http://dx.doi.org/10.1134/S0020441216030192.

Lario, D., 2012. Estimation of the solar flare neutron worst-case fluxes and fluences for missions traveling close to the Sun. Space Weather. 10, S03002. http://dx.doi.org/10.1029/2011SW000732.

Lawrence, D.J., Feldman, W.C., Goldsten, J.O., Peplowski, P.N., Rodgers, D.J., Solomon, S.C., 2014. Detection and characterization of 0.5–8 MeV neutrons near mercury: Evidence for a solar origin. J. Geophys. Res.: Space Phys. 119 (5), 150–171. http://dx.doi.org/10.1002/2013JA019037.

Ligenfelter, R., Flamm, E., Canfield, E., Kellman, S., 1965. High-energy solar neutrons: 1. Production in flares. J. Geophys. Res. 70, 4077–4086. http://dx.doi.org/10.1029/JZ070I017P04077.

Lockwood, J., Debrunner, H., Ryan, J., 1997. The relationship between solar flare gamma-ray emission and neutron production. Sol. Phys. 173, 151–176. http://dx.doi.org/10.1023/A:1004908209975.

Marafini, M., Gasparini, L., Mirabelli, R., Pinci, D., Patera, V., Sciubba, A., et al., 2017. MONDO: a neutron tracker for particle therapy secondary emission characterisation. Phys. Med. Biol. 62 (8), 3299–3312. http://dx.doi.org/10.1088/1361-6560/aa623a.

Massimi, C., Musumarra, A., Leone, F., Pellegriti, M., Romano, F., Spighi, R., Villa, M., 2022. RIPTIDE—an innovative recoil-proton track imaging detector. J. Instrum. 17, http://dx.doi.org/10.1088/1748-0221/17/09/C09026.

McConnell, M., 1994. An overview of solar flare results from COMPTEL. In: Ryan, J.M., Vestramd, W.T (Eds.), In: AIP Conf. Proc, vol. 294, p. 21. http://dx.doi.org/10.1063/1.45193.

McConnell, M., Bennett, K., Forrest, D., Hanlon, L., Ryan, J., Schönfelder, V., Swanenburg, B.N., Winkler, C., 1993. Comptel observations of solar flare gamma rays. Adv. Space Res. 13, 245. http://dx.doi.org/10.1016/0273-1177(93)90485-T.

Mitrofanov, I., Kozyrev, A., Lisov, D., Litvak, M., Malakhov, A., Mokrousov, M., Benkhoff, J., Owens, A., Schulz, R., Quarati, F., 2021. The mercury Gamma-ray and neutron spectrometer (MGNS) onboard the mercury planetary orbiter of the BepiColombo mission: Design updates and first measurements in space. Space Sci. Rev. 217, 67. http://dx.doi.org/10.1007/s11214-021-00842-7.

Mor, I., Vartsky, D., Dangendorf, V., Tittelmeier, K., Goldberg, M., Bar, D., Brandis, M., 2017. Automatic detection of recoil proton tracks and background rejection in liquid scintillator-micro-capillary-array fast neutron spectrometer. J. Instrum. 12, C12022. http://dx.doi.org/10.1088/1748-0221/12/12/C12022.

Muraki, Y., Koga, K., Goka, T., Matsumoto, H., Obara, T., Okudaira, O., Shibata, S., Yamamoto, T., 2012. Measurement by FIB on the ISS: two emissions of solar neutrons detected? Adv. Astron. 2012, 379304. http://dx.doi.org/10.1155/2012/379304.

Murphy, R., Kozlovsky, B., 2017. Neutron production in solar flares by reactions of accelerated 3He. Astrophys. J. 851, 102. http://dx.doi.org/10.3847/1538-4357/aa9ab6.

Murphy, R., Kozlovsky, B., Share, G., 2012. The production of low-energy neutrons in solar flares and the importance of their detection in the inner heliosphere. Astrophys. J. Suppl. Ser. 202, 3. http://dx.doi.org/10.1088/0067-0049/202/1/3.

Musumarra, A., Leone, F., Massimi, C., Pellegriti, M.G., Romano, F., Spighi, R., Villa, M., 2021. RIPTIDE: a novel recoil-proton track imaging detector for fast neutrons. J. Instrum. 16, C12013. http://dx.doi.org/10.1088/1748-0221/16/12/C12013.

Musumarra, A., Patronis, N., Massimi, C., Pellegriti, M.G., Papanikolaou, D., 2024. Towards the next generation of detectors for n-gamma capture reactions at nTOF (CERN). EPJ Web Conf. 304, 01009. http://dx.doi.org/10.1051/epjconf/202430401009.

Nolfo, G., Bruno, A., Dumonthier, J., Liceaga-Indart, I., Legere, J., Messner, R., Mitchell, J., Ryan, J., Suárez, G., Tatoli, T., 2019. Solar neutron tracking (SONTRAC) concept. In: Proceedings of the 36th International Cosmic Ray Conference — Proceeding of Science. p. 358. http://dx.doi.org/10.22323/1.358.1074.

Papanikolaou, D., 2024. Neutron Capture Reactions for Nuclear Astrophysics: Development & Characterization of an Innovative Detection Setup Based on Trans-Stilbene Organic Scintillators (Master's Thesis). https://olympias.lib.uoi.gr/jspui/handle/123456789/38242.

Papanikolaou, D., Musumarra, A., Pellegriti, M.G., Patronis, N., 2025. Neutron capture reactions for nuclear astrophysics: Development & characterization of an innovative detection setup based on trans-stilbene organic scintillators. HNPS Adv. Nucl. Phys. 31, 1. http://dx.doi.org/10.12681/hnpsanp.7995.

Patronis, N., Mengoni, A., for the n_TOF collaboration, 2023. Status report of the n_TOF facility after the 2nd CERN long shutdown period. EPJ Tech. Instrum. 10, 13. http://dx.doi.org/10.1140/epjti/s40485-023-00100-w.

Pisanti, C., Berardi, A., Console Camprini, P., Giacomini, F., Massimi, C., Mengarelli, A., Musumarra, A., Pellegriti, M., Ridolfi, R., Spighi, R., Terranova, N., Villa, M., 2024. Riptide: a proton-recoil track imaging detector for fast neutrons. J. Instrum. 19, C02074. http://dx.doi.org/10.1088/1748-0221/19/02/C02074.

Share, G.H., Murphy, R.J., Tylka, A.J., Dennis, B.R., Ryan, J.M., 2015. Misidentification of the source of a neutron transient detected by MESSENGER on 4 2011. J. Geophys. Res.: Space Phys. 120, 1. http://dx.doi.org/10.1002/2014JA020663.

Shibata, K., Magara, T., 2011. Solar flares: Magnetohydrodynamic processes. Living Rev. Sol. Phys. 8, 1–99. http://dx.doi.org/10.12942/LRSP-2011-6.

Song, Z., Sun, S., Ouyang, X., 2020. A simulation study of a high-resolution fast neutron imaging detector based on liquid scintillator loaded capillaries. Radiat. Detect. Technol. Methods 4, 153–160. http://dx.doi.org/10.1007/s41605-020-00164-2.

Valle, S.M., Battistoni, G., Patera, V., Pinci, D., Sarti, A., Sciubba, A., et al., 2017. The MONDO project: A secondary neutron tracker detector for particle therapy. Nucl. Instrum. Methods Phys. Res. Sect. A: Accel. Spectrometers Detect. Assoc. Equip. 845, 556–559. http://dx.doi.org/10.1016/j.nima.2016.05.001.

Vilmer, N., MacKinnon, A., Hurford, G., 2011. Properties of energetic ions in the solar atmosphere from gamma-ray and neutron observations. Space Sci. Rev. 159, 167–224. http://dx.doi.org/10.1007/s11214-010-9728-x.

Weldon, Jr., R.A., Mueller, J.M., Awe, C., Barbeau, P., Hedges, S., Li, L., Mishra, M., Mattingly, J., 2020. Characterization of stilbene's scintillation anisotropy for recoil protons between 0.56 and 10 MeV. Nucl. Instrum. Methods Phys. Res. A 977, 164178. http://dx.doi.org/10.1016/j.nima.2020.164178.

Zaitseva, N., Glenn, A., Carman, L., Hatarik, R., Hamel, S., Faust, M., Schabes, B., Cherepy, N., Payne, S., 2011. Pulse shape discrimination in impure and mixed single-crystal organic scintillators. IEEE Trans. Nucl. Sci. 58, 3411. http://dx.doi.org/10.1109/TNS.2011.2171363.

Zaitseva, N., Glenn, A., Carman, L., Martinez, H.P., Hatarik, R., Klapper, H., Payne, S., 2015. Scintillation properties of solution-grown trans-stilbene single crystals. Nucl. Instrum. Methods Phys. Res. A 789, 8–15. http://dx.doi.org/10.1016/j.nima.2015.03.090.

Zaitseva, N., Glenn, A., Mabe, A., Carman, L., Payne, S., 2020. New solid-state organic scintillators for fast and thermal neutron detection. Int. J. Mod. Phys.: Conf. Ser. 50, 2060003. http://dx.doi.org/10.1142/S2010194520600034.

Zhou, J., Gaughan, N., Becchetti, F.D., Torres-Isea, R.O., Febbraro, M., Zaitseva, N., Di Fulvio, A., 2022. Light output quenching in response to deuterium-ions and alpha particles and pulse shape discrimination in deuterated trans-stilbene. Nucl. Instrum. Methods Phys. Res. A 1027, 166287. http://dx.doi.org/10.1016/j.nima.2021.166287.